Deep–Sea Research I 196 (2023) 104021

Contents lists available at ScienceDirect

Deep-Sea Research Part I

journal homepage: www.elsevier.com/locate/dsri

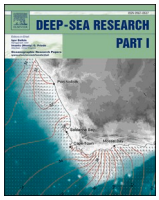

Internal tidal sloshing and a non-linear wave source away from topography

Hans van Haren

NIOZ Royal Netherlands Institute for Sea Research, P.O. Box 59, 1790, AB, Den Burg, the Netherlands

ARTICLE INFO

Keywords:
Kilometer long thermistor string
Mooring observations
Internal tide-phase and -amplitude tracing
>100 m tall Breaker zone
Off-slope generation
Mount Josephine

ABSTRACT

The ocean-interior shows omnipresent internal wave motions whose importance becomes more and more acknowledged for deep mixing across the stable vertical density stratification for heat and suspended matter redistribution. To observationally study vertical propagation variations of internal tides away from a steep topographic slope, a >1-km long mooring with 760 high-resolution temperature sensors was deployed at 2380 m depth halfway Mount Josephine NE-Atlantic Ocean for 4 months. In the lower 150 m above the seafloor, internal waves slosh, become highly non-linear and break vigorously, every tidal cycle. After signal separation using semidiurnal band-pass and harmonic filters, the vertical phase propagation shows: 1. Phase differences of 90° are observed in isotherms and cross-slope currents over typically 600 m in the vertical, 2. Non-linearity is already found in harmonic records that describe 300-m large-scale internal tides, 3. Non-uniform thin-layer stratification causes about 50% of the semidiurnal variance in small-scales, 4. Upward internal tide propagation starts at the top of non-linear wave breaking, 5. Downward propagation from above leading to energy-focusing at 700 m above the ocean-floor and about 700 m below the nearest seamount-ridge generates interior hydraulic jumps during spring tide.

1. Introduction

Amongst the main generators of internal waves are tidal motions, after interaction with the omnipresent ocean-floor topography (LeBlond and Mysak, 1978; Garrett and Kunze, 2007). Acknowledging that internal wave propagation is an essentially three-dimensional (3D-x,y,z) phenomenon in contrast with 2D-x,y propagating surface waves, one type of (2D-z,x) model assumes that major internal wave-generation occurs at ocean-floor slopes γ that 'critically' match the slope of internal tide energy propagation (e.g., Pingree and New, 1991; Gerkema, 2002; Lamb, 2004). Such model results, e.g., in semidiurnal lunar M_2 internal (baroclinic) tide being generated from an M_2 surface (barotropic) tide. The stratification supporting internal waves in these models is either constant or a smoothly varying function of the vertical z (commonly monotonically decreasing with depth), whilst being fixed in t, x, y. At the same critical slopes incoming internal tidal energy is trapped, because wave energy cannot (theoretically) reflect from the matching topography slope, and large turbulent mixing is expected (e.g., Slinn and Riley, 1996). In this paper, we are concerned with internal tide generation from a large seamount above a steep slope where considerable internal wave breaking occurs. The observational study uses a densely instrumented, more than 1 km long mooring with high-resolution sensors.

From laboratory models (e.g., Mowbray and Rarity, 1967) it has been recognized that internal wave energy is contained in beams or rays (regions of large amplitude) that propagate along certain 'characteristic' paths having a slope to the horizontal that depends on N(x, y, z, t), the local buoyancy frequency, and f(φ), the local inertial frequency at latitude φ. In sufficiently stratified waters N » f, downward internal-wave phase propagation (a phase advance in time with increasing depth) implies upward energy propagation, and vice versa (LeBlond and Mysak, 1978). Thus, the monitoring of vertical phase differences also provides insight in energy propagation, whereby it is noted that directions of phase and energy propagation are parallel in the horizontal.

In the (Mowbray and Rarity, 1967) constant-N experiment, fainter beams at larger angles to the horizontal were recognized that corresponded to a higher harmonic frequency. Away from the source, internal waves rapidly disperse. These beams are well-separated in space and waves do not proceed from one beam to the other (Dauxois et al., 2017). If an observational antenna of sufficient length would be moored in the laboratory model, it would thus register different energy at different harmonic frequencies at various heights above the basin-floor.

Oceanic wave beams are the small vertical scale component of propagating internal waves that radiate from ocean-floor topography during the conversion of barotropic (surface) to baroclinic (internal) tide in the stratified ocean (Bell, 1975). Initially, main sources were

E-mail address: hans.van.haren@nioz.nl.

https://doi.org/10.1016/j.dsr.2023.104021
Received 14 October 2022; Received in revised form 28 February 2023; Accepted 5 March 2023
Available online 8 March 2023

considered at the continental shelf edge (LeBlond and Mysak, 1978; Pingree and New, 1991). More recently, abrupt topography like mid-ocean ridges are also thought responsible for considerable internal tide generation (Garrett and Kunze, 2007).

The energy conversion rate depends on the value of N and on the topography slope for barotropic tidal current component W (Baines, 1982; Gerkema et al., 2004). Ocean-floor slope criticality with most energy conversion occurs when the slope to the horizontal of internal wave beams is close to that of γ (Balmforth and Peacock, 2009). As propagating internal wave frequencies (σ) are generally found in the band $f \leq \sigma \leq N$, their beam-slopes β depend on local f, N and σ: $\beta = \sin^{-1}((\sigma^2\text{-}f^2)^{1/2}/(N^2\text{-}f^2)^{1/2})$, e.g., LeBlond and Mysak (1978). An ocean-floor slope is supercritical when $\gamma > \beta$, steeper than the internal wave slopes of interest. An ocean-floor slope is subcritical when $\beta > \gamma$.

However, spatially and temporally monochromatic internal wave trains do not well describe most geophysical internal waves (Sutherland, 2013). This shows in numerical models even for N(z), in which phase and amplitude changes are no longer found across beams but throughout a basin over short scales (Gerkema, 2002). Indeed, oceanic observations have shown higher tidal harmonics in consistent sequences in descending order at various deep-ocean locations reflecting highly non-linear 'broadband' waves (van Haren et al., 2002, van Aken et al., 2007). Observations have also shown that internal wave beams appear 'patchy' in the ocean rather than showing a confined high-energy range (Lien and Gregg, 2001, van Haren et al., 2010; Johnston et al., 2011).

These observations suggest the model of a constant-N ocean is too simplified and effects of variable N(x, y, z, t) in thinner and thicker layers on internal wave generation, propagation and interaction are not to be overlooked. The stable vertical density stratification imposed by solar radiation in the ocean is not fixed but varies in x, y, z, t. It is modified on the large scale by basin-wide circulation, on medium scale by eddies that spin off boundary flows and on small scales by internal wave straining. This leads to a complex of non-uniform stratification through which internal waves of various scales propagate, or become trapped (e.g., for $\sigma < f$, $\sigma > N$).

Detailed observations of internal wave-induced turbulence have demonstrated particularly strong diapycnal mixing during short bursts of incoming nonlinear waves and bores above steeply sloping topography (e.g., Grue et al., 2000; Klymak and Moum, 2003; Winters, 2015; Sarkar and Scotti, 2017) and near the top of seamount(-ridge)s (e.g., Legg and Klymak, 2008). Nonlinear bores have important effects on sediment resuspension (Hosegood et al., 2004) and occur every tidal period although with varying amplitude and time of arrival. It led to the suggestion that internal wave generation above topography may be a rather broadband phenomenon generating non-linear internal tides at the source rather than monochromatic waves (van Haren, 2006). Internal-wave generation by turbulence has been suggested in the stratified layer below the mixing layer near the sea-surface (Gregg et al., 1985; Moum et al., 1989).

Frontal bores occurring every tidal period are accompanied by O(10 min) pulses of baroclinic vertical current component $w \approx 0.1$ m s^{-1} » W, and irregular small-scale waves superimposed on an asymmetric tidal signal. The energy-conversion rates -ρ<bW> and -ρ<bw>, in which b denotes buoyancy, ρ a reference density and <> tidal averaging, to internal tidal energy will also depend on internal tides generated elsewhere and thus modifying b for band-broadening away from monochromatic waves. This may be related to the generation of higher tidal harmonics as shown in numerical modelling taking into account nonlinear effects (e.g., Lamb, 2004). If so, it may explain the intermittent character of internal tides being generated from non-deterministic baroclinic motions rather than from deterministic barotropic tides. Internal tides generated from the latter require further interactions with other waves, currents or varying stratification to produce intermittency that is typically observed in the ocean (Wunsch, 1975).

In this paper, we are curious what is observable using a mooring equipped with an unusually large number of 760 high-resolution temperature (T-)sensors that was moored above a steeply sloping ocean-floor of Mount Josephine in the Northeast-Atlantic Ocean for 4 months. An overview of the data is presented in van Haren (2022). It builds further on 100-200 T-sensor multiple-site moorings above the same side the seamount and demonstrating the largest turbulence over steep slopes that are supercritical for semidiurnal internal tides (van Haren et al., 2015; van Haren, 2017). The present purpose is to provide insight in connections between the seamount-slope, internal wave breaking exceeding 100-m above the ocean-floor, and internal tide generation at the top of the breaker zone or at the ocean-floor proper. Vertical phase relationships are inferred for tides extracted via harmonic analysis and band-pass filtering, which also separates barotropic motions from the records.

2. Technical details

'KmT', an 1140-m long T-sensor array was deployed for four months in 2019 at 37° 00′N, 013° 44.5′W, with local ocean-floor at z = −2380 m on the eastern flank of Mount Josephine (Fig. 1a), about 400 km southwest of Lisbon (Portugal). KmT was the follow-up of a similar but shorter 400-m array that was deployed four years earlier at a site 3.5 km to the East, in about 500-m shallower waters. Its data will be discussed briefly to support the data from KmT.

For the study on internal wave-turbulence from near to far above a sloping ocean-floor, 760 NIOZ4 high-resolution T-sensors were taped to the nylon-coated 0.006-m outer diameter steel mooring cable and to an inline-frame approximately halfway the cable. The T-sensors were at 1.5-m vertical intervals between z = −1234 and −2372 m. A 4.2-kN elliptic buoy was at −1105 m, 100 m above a similar second buoy holding a downward looking 75-kHz RDI/Teledyne Longranger acoustic Doppler current profiler (ADCP) with 20° acoustic beam-slant angle to the vertical. The inline-frame held a second 75-kHz (deep-water version) downward looking ADCP to cover the lower 600-m range of the T-sensors.

The ADCPs sampled at a rate of once per 900-s average values in 60 vertical bins of 10 m. Due to sidelobe reflection, the nearest bin of good data is 45 m above the seafloor. The horizontal beam spread averaging of current components varied between about 15 and 420 m. Such scales of averaging are larger than the sizes of most turbulent overturning in the ocean. Turbulent overturns are thus not well resolved by these ADCPs and they merely provide a coarsely sampled impression of major (tidal) water-flow motions. The error in one 900-s sample of current amplitude is 0.014 m s^{-1}, so that at semidiurnal frequencies it is 0.002 m s^{-1} following random statistics. Vertical currents are generally well-resolved and extend above noise level between f and N. For $\Delta z = 10$-m-scale shear amplitude $|S| = ((\Delta u/\Delta z)^2+(\Delta v/\Delta z)^2)^{1/2}$ however, the instrumental noise level is high throughout, except at near-inertial frequency. It is not considered here.

In contrast, the T-sensors sampled at a rate of once per 1 s and resolve the most energetic turbulent overturning scales down to the Ozmidov scale of stratified turbulence.

The mooring assembly was held tautly upright with net 5-kN buoyancy and the 8-kN bottom-weight generated net-anchoring with approximately 3 kN. The ADCPs' tilt and pressure sensors demonstrated that even under maximum 0.3 m s^{-1} current-flow speeds the top of the mooring deflected little, vertically by < 0.2 m and horizontally by < 20 m. Shipbone SeaBird SBE9plus Conductivity-Temperature-Depth (CTD) data were obtained near the mooring in cross-slope direction.

2.1. Site characteristics

The average local ocean-floor slope of $\gamma = 9\pm1°$ is scale-dependent. When computed using a 6-km horizontal scale, the larger scale slope is about 8°. When computed using a 2-km horizontal scale, local slopes go up to 10°. At the mooring site, γ » $\beta_{M2} = 4 \pm 1.5°$ for dominant M_2 internal tide beam-characteristics of energy propagation (Fig. 1) under

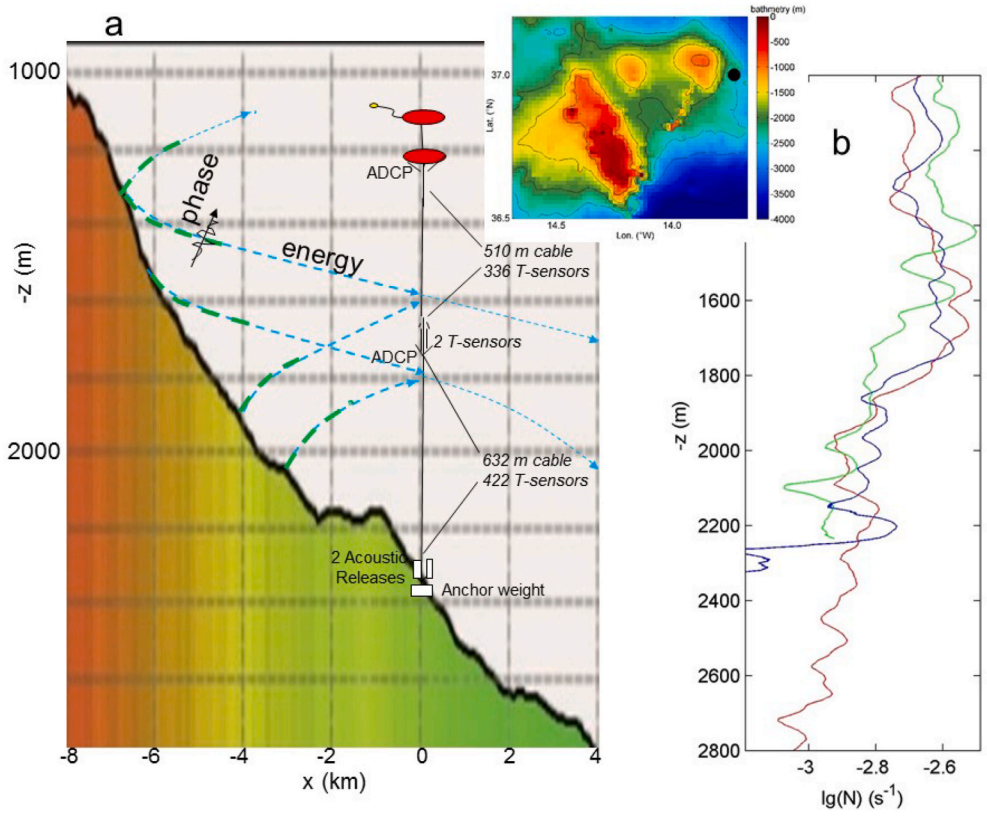

Fig. 1. Site information. (a) East-west Multibeam transect along 37 °00′N of the bathymetry of Mount Josephine around the mooring site, drawn in an aspect ratio of vertical:horizontal = 8:1. The mooring outline is included, together with schematics of a few-only (~semidiurnal) internal tide beam-characteristics of energy propagation (blue-dashed) from upper and lower slope and, in green-dashed, the spatial extent of internal wave breaking following a model by Winters (2015). The insert shows the bathymetry from the 1′-version of Smith and Sandwell (1997), with the black dot indicating the mooring site. (b) Logarithm of buoyancy frequency computed over 100-dbar (~100-m) vertical intervals from CTD-profiles across the slope at water-depths of 2200 m (green), 2400 m (blue) and 3200 m (red).

mean local stratification conditions resulting in $N = 1.8 \pm 0.6 \times 10^{-3}$ $s^{-1} \approx 20f$. The site is therefore considered supercritical for freely propagating internal tidal waves.

Over the >1 km vertical range of T-sensors, the beam-slopes vary by a factor of 1.8, due to the vertical decrease with depth in mean stratification (outside large-turbulence zones just above topography). In the interior, internal wave beams generally slope steeper at greater depths. At the present site however, stratification has a local maximum between $-1800 < z < -1350$ m and local minima in the 200–400 m thick layer above the seafloor as evident from snapshot CTD-profiles (Fig. 1b). Hypothetically, for example, for the intermediate vertical range between −1600 and −1800 m, propagating waves reaching the mooring line in that interval can originate either from [−1300, −1500] m or from [−1900, −2050] m on the seamount slope (Fig. 1). For comparison, modelled horizontal extent of breaking internal wave turbulence above a supercritical slope reaches about 1 km horizontally from the slope (Winters, 2015). This breaking potentially does not reach the mooring line in the intermediate depth-range. Most intense breaking is expected to reach the mooring in the lower 200 m above the seamount slope.

The top of the mooring and the uppermost sensors were about 120 and 240 m below the crest of the nearest ridge at z = −980 m, respectively. The ridge is part of nearest sub-summit at −800 m, about 14 km west-northwest of the mooring. Mount Josephine's absolute summit extends up to −250 m. The top of the mooring reached into waters of the Mediterranean Sea outflow, potentially between about −1000 and −1400 m, so that partially salinity-compensated apparent density inversions were occasionally registered in the upper range of T-sensors when a Mediterranean outflow lens passed (Hebert et al., 1990). Non-turbulence-induced artificial inversions are recognizable in the T-records as thin-layer instabilities lasting longer than a day. They can be distinguished from genuine turbulent overturning which are not expected to last longer than the inertial period (e.g., Dale et al., 2006). Mediterranean outflow intrusions are thus easily detectable and they are excluded from turbulence analyses.

2.2. Temperature sensors

NIOZ4 are self-contained T-sensors with a precision better than 5×10^{-4}°C after drift-correction, a drift of about 1×10^{-3}°C mo^{-1} after aging, and a noise level of $<1 \times 10^{-4}$°C (van Haren, 2018). Every 4 h, a synchronization pulse is sent via induction to all T-sensors of which the internal clock is adjusted to a single standard clock, so that the entire T-sensor range is sampled with less than 0.02 s delay between the sensors. In comparison with previous smaller moorings, the synchronizer for KmT is housed in a larger container holding twice the amount of batteries. The synchronizer is attached to the inline-frame, in the middle of the two T-sensor cable sections. The inline-frame is non-swiveled and attached directly via shackles to the mooring cables above and below, because the synchronization pulse is sent via flexible electrician's wire to the mooring cables. The wire is not to be cut by a potentially spinning frame. Two T-sensors are attached to the inline-frame and synchronized via the wire.

Although previously the synchronization was successfully used up to 400-m cable-length (van Haren, 2017), the present result for two sections of 510 and 630-m cable-lengths was unexpected as 93 out of 760 T-sensors showed difficulties in synchronization. A problem showed in the coating of the cable, which was scratched in some places causing electric leakage. But the range seemed to be the largest problem, as about 80 of the 93 failing synchronizations occurred at a distance of more than 400 m from the synchronizer. This distance is clearly the limit of the present electronics set-up for synchronization in seawater.

Failing synchronization is corrected by searching for the moment of acoustic mooring release upon recovery, which provides a time-stamp to within 1 s as the rather slim and heavily buoyant mooring ascents at a speed of about 1.3 m s^{-1}. The average correction to this time-stamp is 8 s over the 4-month record. The synchronizations to the time-stamp are interpolated over the entire 4-month record and implemented when they exceed half the (sub-)sampling interval for the portion of the record investigated. Remaining errors are within 1 s for these 93 T-sensors,

which is negligibly small on a tidal scale lasting half-one day and also on the energy-containing turbulence scales that typically last 1000–3000 s. Some 53 T-sensors demonstrated electronics, data storage, battery, noise or calibration problems. The data from these sensors are linearly interpolated between those from neighboring T-sensors.

2.3. Post-processing methods

The moored T-data are converted into Conservative Temperature data Θ (IOC, SCOR, IAPSO, 2010). They are used as tracer for density anomaly variations following the relation $\delta\sigma_2 = \alpha\delta\Theta$, $\alpha = -0.053 \pm 0.01$ kg m^{-3} °C^{-1}, where α denotes the linear coefficient of local fit and subscript 2 the reference pressure level of 2×10^7 N m^{-2}. This relation is established from shipborne CTD-data between 1250 and 2400 m obtained within 1 km horizontally from the KmT-site. Thus, given the reasonably tight density-temperature relationship, the number of T-sensors and their vertical spacing of 1.5 m, in combination with their low noise level, allows to calculate turbulence values like dissipation rate ε via the reordering of unstable overturns for every 1-s sampled vertical profile (Thorpe, 1977). Reordered profiles are used to compute 1.5-m-small-scale buoyancy frequency N_s. Further details on the computation of turbulence values from moored T-sensors are given in (van Haren, 2017, 2018).

The >1-km vertical range of densely spaced moored T-sensors also allows for an investigation of small and large baroclinic (vertically inhomogeneous) internal waves. Such analysis requires separation from barotropic (vertically homogeneous) surface waves in the same band, notably tidal motions. Barotropic tidal motions are considered highly deterministic, with long wavelength for their waves. Baroclinic tidal motions have finite (spectral) bandwidth and short wavelengths and are known for their intermittency or highly variable occurrence in time (Wunsch, 1975).

To separate these tidal motions, two methods can be used. First, the vertical average data can be considered as barotropic, and the residue from the original times series as baroclinic. Unfortunately, KmT covers only half the local water column, and a proper vertical average cannot be established. Second, a sharp band-pass filter like harmonic analysis (Dronkers, 1964) can be used to separate, per vertical level, the deterministic part of the signal. The baroclinic signal per vertical level is obtained by subtracting the harmonic from the original signal. Harmonic analysis is only useful when the time series are considerably longer than the typical intermittency period of a few days for a baroclinic tide, at least longer than a fortnight and preferably longer than a month. Harmonic analysis also has a disadvantage as the deterministic signal may contain some of the baroclinic signal in a time series. In general, the baroclinic portion in a sharp harmonic filter is limited as internal wave energy is distributed over a wider (flat, albeit finite-width) band. Unfortunately, harmonic analysis cannot be associated with error analysis. At least, not in random-statistics sense and it is nonsensical to do so for pure deterministic signals. However, what is commonly done, as a sort of best practice, is to take the standard deviation of the residual signal, which results after subtracting the harmonic from the original signal, as a measure for error. This only works in areas where deterministic signals are dominant, such as in shallow water tides, because the residuals may reflect other non-random oceanographic dynamics such as baroclinic tides.

Here, harmonic analysis (Pawlowicz et al., 2002) will be applied to the semidiurnal signal that is band-pass filtered between [1.74, 2.12] cpd (short for cycles per day) for each of the 760 T-records. The band-pass filtered records contain signals at all scales including the smallest, presumably intermittent scales. The harmonic analysis uses all statistically independent constituents within that frequency band for a 4-month time series. Three different records will be compared: the harmonic records for all independent constituents, the harmonic records for M_2 and solar S_2 only, and the band-pass filtered records. The comparison focuses on vertical phase differences and internal (non-)linearity in time-depth images and provides an indication of errors to (in) consistencies.

3. Observational results

3.1. Overview of mooring data

In Fig. 2, a 2-d/1146-m time/vertical overview is given of temperature and current observations around spring tide. Conservative Temperature (Fig. 2a) demonstrates >100-m amplitude of semidiurnal tidal isotherm-excursions in the t,z-plane that are largest near the ocean-floor. Away from the ocean-floor, not only excursion-amplitudes decrease, but also the phase of the tidal motions differs by about a quarter-period with that of the deepest isotherm. On top of the semidiurnal periodicity, shorter period variations are seen, which, however, may occur on a semidiurnal periodic interval, e.g., between $-1800 < z < -1600$ m.

The short-period variations in this 200-m vertical range appear with turbulent overturns, at about $z = -1700$ m, 700 m above the local ocean-floor (Fig. 2b). These interior overturns are not directly associated with internal wave breaking observed during a different phase of the tide in the lower 200 m above the ocean-floor. This lower 200-m high turbulence zone is somewhat larger than the modelled vertical extent of a sloshing internal tide (Winters, 2015). This zone is considerably larger than the Ekman layer of frictional flow, which is even during the strongest turbulence smaller than 35 m from the seafloor. Thus, the ADCPs have not sampled the frictional flow layer, as it is less than the range of sidelobe contamination above the seafloor.

Largest turbulence dissipation rate occurs in weak stratification, but rapid restratification is observed immediately surrounding such zones (Fig. 2c). Every semidiurnal period, the turbulence commences at the ocean-floor just after the turn of tide to onslope motion (Fig. 2d). This is different from modelling results of lee-wave breaking near the top of a seamount-ridge, where turbulence occurs during the downslope phase and halts just before the flow reversal (Legg and Klymak, 2008). The thereby enhanced turbulence reaches down to about 400 m below the ridge-crest (which is well above the turbulence patches observed here as the top of the mooring was about 300 m below the nearest ridge-crest.)

Not only isotherms but also the cross-slope current component indicate a relatively large phase difference of more than 90° in the vertical. From about $z = -1700$ m co-phases suggest a downward phase propagation towards the ocean-floor as well as an upward phase propagation towards the surface, best visible around day 139.6 in Fig. 2d. This will be further investigated using harmonic analysis and band-pass filtering below.

The along-slope current component shows less clear vertical phase propagation. Its amplitude seems to increase in the range $-2335 < z < -2100$ m, but only in southward direction. After subtraction of the tidal motions, a 'residual' flow of $v = -0.06$ m s^{-1} results for this two-day period. The residual flow will be important for potential redistribution of suspended matter when that is whirled up by the turbulence induced by breaking internal waves. The tidal flow components have approximately the same amplitudes for $z < -2280$ m and $z > -1800$ m, as will become clearer below.

The high-resolution temperature observations show thin-layer stratification throughout (Fig. 2c), down to the 1.5-m sampling level. This is likely due to straining by the internal wave activity with associated shear-turbulence. High-frequency internal wave activity may result from the large turbulence at the seafloor, e.g. after the passage of a bore. Somewhat less likely, closer to the topography the turbulence may proceed some distance <1 km (Winters, 2015) along isopycnals. The coarser sampled horizontal current components (Fig. 2d and e) also show layering O(10) m, which supersedes the larger tidal scales both in time and vertical. Obviously, the small-scale motions have a baroclinic character as these contribute to intermittency despite their occurrence at quasi-semidiurnal periodicity. The vertical current component (Fig. 2f) changes character at about $z = -2000$ m, above which it is dominated by

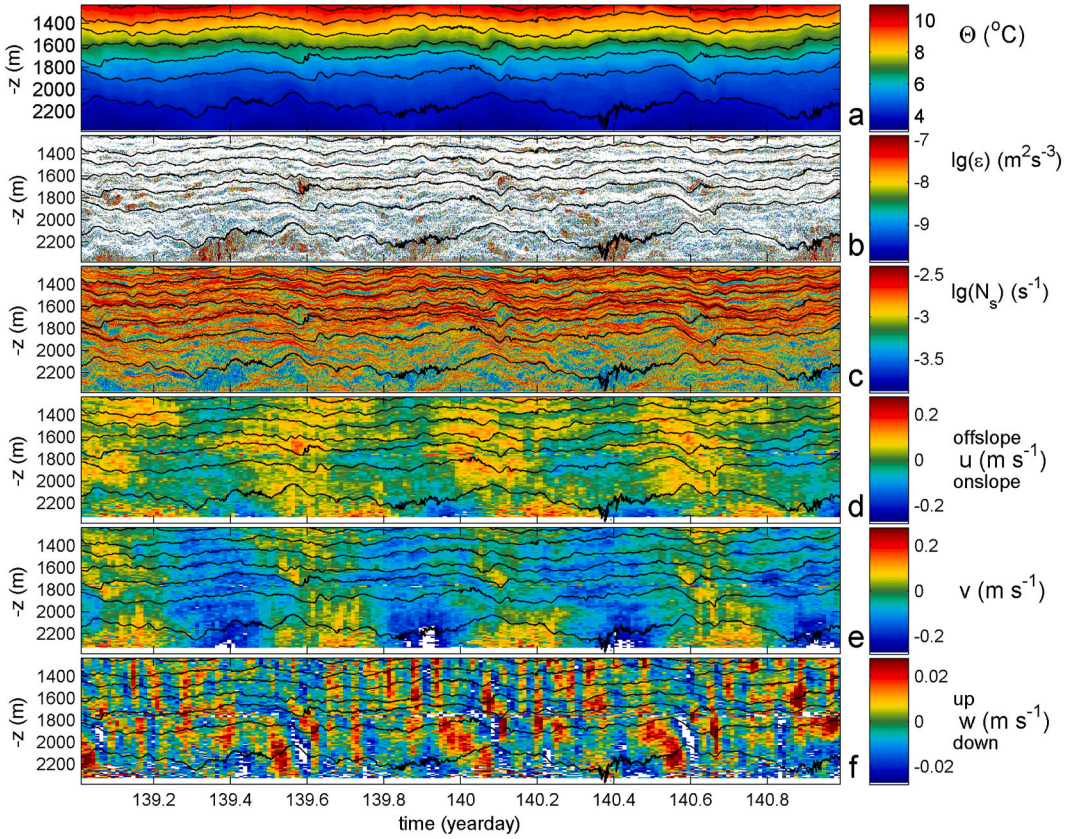

Fig. 2. Data-detail of two days around spring tide. In all panels, the ocean-floor is at the level of the x-axis. (a) Conservative Temperature from KmT-sensor data subsampled at 0.1 Hz, with black contours at 1 °C intervals. These contours are repeated in all subsequent panels, for reference. (b) Logarithm of non-averaged turbulence dissipation rate from the data in a. (c) Logarithm of 1.5-m-scale buoyancy frequency calculated from the vertically sorted version of a. (d) East-West horizontal current component from 900-s sampled, 10-m binned ADCP-data (ADCP-data are contaminated in the range up to 45 m above the seafloor due to sidelobe reflection). (e) As d., but for North(positive)-South(negative) horizontal current component. (f) As d., but for vertical current component measured by ADCP. Note the different scale compared to d., e.

internal waves near N ≈ 25 cpd, or 1 h periodicity. For z < −2000 m, semidiurnal periodicity is visible. However, also in these w small-scale motions supersede the larger structures and a quasi-semidiurnal appearing intermittency is observed.

3.2. Semidiurnal motions and scales

A nine-day plot over the 1140-m vertical range of observations demonstrates the non-barotropic character of 4-month harmonic records (Fig. 3a). While a neap-spring variation reflecting the interaction between deterministic M_2 and S_2 is observed throughout the vertical, the precise occurrence of neap- (or spring-)tide varies considerably. Third largest semidiurnal tidal constituent N_2 is indistinguishable from the level of flat internal wave band. Also, the phase and amplitude of semidiurnal isotherm-excursions differs. In the upper 600 m of the T-sensor range, M_2 and S_2 are dominant as their excursions are almost indistinguishable from those describing the full set of statistically independent harmonic constituents in the semidiurnal band. (Compare the two isotherms at z = −1600 m). In the lower 500 m of the T-sensor range however, the full set of harmonic constituents displays excursions that show a more non-linear, cnoidal character rather than linear sinusoidal motions. These observations suggest that non-linearity may already be incorporated in quasi-deterministic (semidiurnal) signals extracted by harmonic analysis, and that the harmonic signals describe large-scale baroclinic motions but not barotropic signals.

The harmonic analysis extracts 50 ± 5% of the temperature variance in the semidiurnal band, as was inferred by comparison with the other 50% 'residual' of the band-pass filtered records (Fig. 3b) after subtraction of the semidiurnal harmonic records (Fig. 3a) from the original records (white isotherms in Fig. 3b). Although the residuals contain considerable high-frequency motions besides non-phase-coupled baroclinic tides by definition, these may occur at semidiurnal periodicity as reported above. Especially around mid-range −1900 < z < −1600 m such semidiurnal periodicity is obvious. As these signals are not captured as quasi-deterministic by harmonic analysis, they are part of the broader semidiurnal band at non-deterministic tidal frequencies. They contribute to intermittency and, considering their finer vertical scales, to smaller baroclinic motions. Such motions are considered to follow from interactions between larger scale internal tides, e.g. propagating in beams, and thin-layer stratification, thereby possibly generating interfacial waves (van Haren and Maas, 2022).

The combination of the larger and smaller scale baroclinic motions is contained in the semidiurnal band-pass filtered signal (Fig. 4). The comparison of Fig. 4a with Fig. 3a subtly shows more non-linear excursions in the former, at all levels including in the upper 600 m of the range. Although the large-scale baroclinic motions appear dominant, the small-scale baroclinic motions reflect the different non-linear deviations from sinusoidal motions in each and every isotherm. This also shows without addition of time-averages per record (Fig. 4b). Most obvious are the thin-layers of near-zero value interrupting the vertical higher amplitude columns during neap-tide. In detail, the columns show small-scale amplitude variations and, by vertical wiggles, phase variations. On larger scales, the layer between −2200 < z < −1800 m shows smaller amplitudes during most of the displayed period compared to the rest of the vertical range.

The large-scale baroclinic motions are best represented by the non-

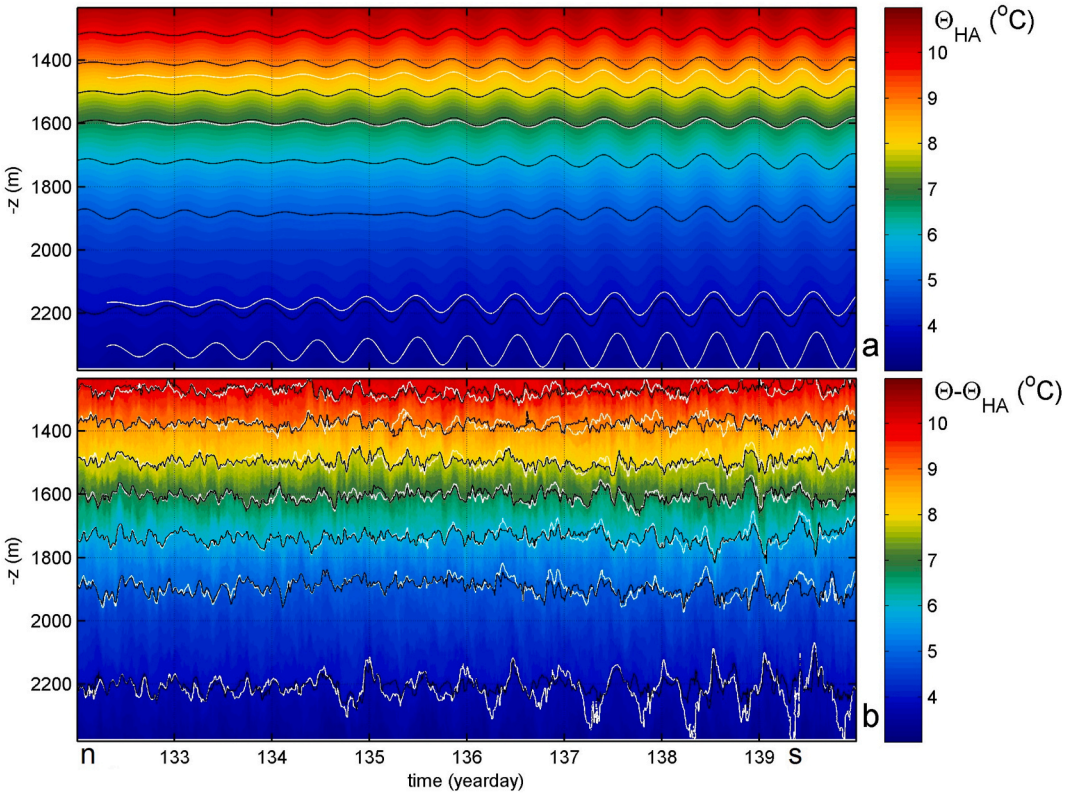

Fig. 3. Time-vertical plots of nine days of KmT-sensor data from neap to spring tide. In all panels, the ocean-floor is at the level of the x-axis. (a) Harmonic analysis using all independent constituents from the semidiurnal (SD) band computed for each of the 760 4-month records. In black, isotherms are given at 1 °C intervals. In white, four isotherms are given from combined lunar M_2 and solar S_2 only, no other SD-harmonics. For comparison with b., data are supplemented with time-mean values of the original records. (b) Residuals after subtraction of harmonic data in a. from original records. The white isotherms are from the original records, for reference. Baroclinic near-seafloor n(eaps) and s(prings) are indicated.

uniform verticality of the columns (Fig. 4b). Every deviation from vertical implies a phase change. Thus, following the large-scales starting around mid-range at about $z = -1800$ m which is the latest occurring in every vertical profile around neaps and earliest around springs, internal tidal energy is transported downward towards the ocean-floor, because phase-propagation is upward, and upward towards the surface, because phase-propagation is downward, around neap-tide (day 132). In contrast during the more energetic (baroclinic) spring-tide (day 139), energy is transported to mid-range, upward from the range below and downward from the range above.

This vertical phase-(and thus energy-) propagation is confirmed in the current components, which reveal consistently similar results best visible in the cross-slope u-current component (Fig. 5). Below $z < -2000$ m, the band-pass filtered semidiurnal currents are mainly directed along the slope, but increasingly turn to cross-slope directions with almost exactly obliquely directed major axis of the current ellipse at $z = -2330$ m, the deepest point of good data. It is expected that the current-ellipse major axis will be directed cross-slope with upslope flow leading a cold-water frontal bore closer to the seafloor, as has been observed above deep-sea sloping topography previously (e.g., van Haren, 2006).

At 100-m scales, variations are added to this pattern, see also the two-day detail in temperature (Fig. 6). Examples are a switch between up- and down-going energy between $-1600 < z < -1400$ m, at which largest amplitudes are found, and down-going energy for $z < -2200$ m which is observed consistently during spring-tide. This may be due to a local focusing of internal tide energy. Such variations are better visible in the band-pass filtered signal (Fig. 6b), but can also be discerned in the harmonic records (Fig. 6a). These observations also follow from 4-month harmonic analysis data that show approximately the same vertical profiles of amplitude and phase, for both M_2 and S_2 separately. This suggests the two constituents are coupled and not found in separate beams. Over a horizontal range of 5 km the vertical variation is only 17 m between them (near the same slope-source).

The variations with time and vertical in direction of internal tide propagation demonstrate a more complex internal wave pattern than is generally modelled using mono-chromatic waves. Even larger complexity is expected when the variations in N(x, y, z, t) are accounted for. Such variations are partially brought about by the breaking and restratifying effects of internal waves. Another side-effect may be that the source of internal waves will vary and may not necessarily be at the ocean-floor, as often modelled for internal tides. The above spring-tide observations suggest a source O(100) m above the ocean-floor, i.e. at the top of variable vertical motions periodically brought about by the non-linear wave breaking. This associates with a previously suggested finite bandwidth source of internal tides (van Haren, 2006) rather a monochromatic wave source.

For consistency check, the observations are compared with similar ones (Fig. 7) computed using data from a smaller 400-m range T-sensor mooring that was deployed at the same latitude but at a slightly shallower ($z = -1890$ m) site in 2015 (van Haren, 2017). From above, the spring-tide data show upward energy propagation, while energy propagates downward between about $-1800 \pm 50 < z < -1625 \pm 25$ m and either upwards or downwards in the lower 20–50 m. Except the ambiguous directions near the seafloor the propagation directions are the same as observed in Fig. 6.

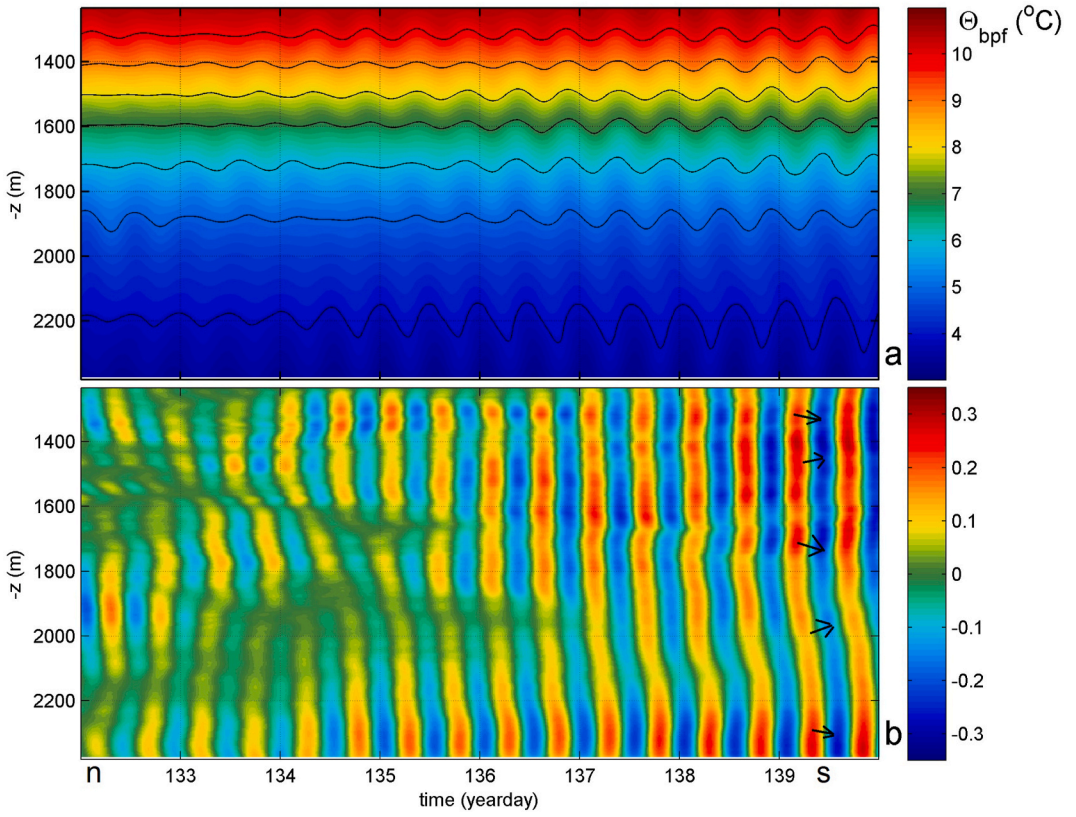

Fig. 4. SD band-pass filtered (bpf) KmT-sensor data. The filter cut-off frequencies are at [1.74 2.12] cpd. (a) Similar to Fig. 3, but for SD-bpf records supplemented with time mean values of the original records, for comparison with Fig. 3. (b) Bpf data only. The arrows indicate possible (vertical) directions of propagating internal tide energy inferred from vertical phase variations. The green shading of near-zero values is attributable to modulations such as during neaps.

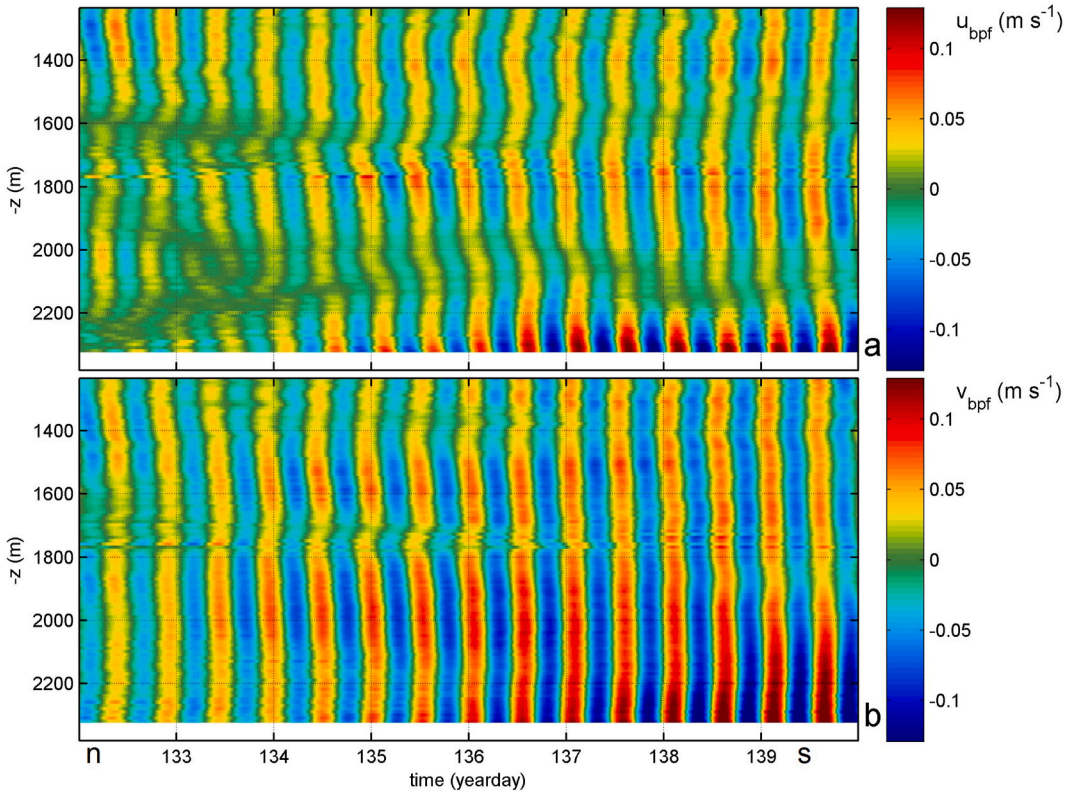

Fig. 5. As Fig. 4b, but for ADCP-measured current components. (a) East-West. (b) North-South.

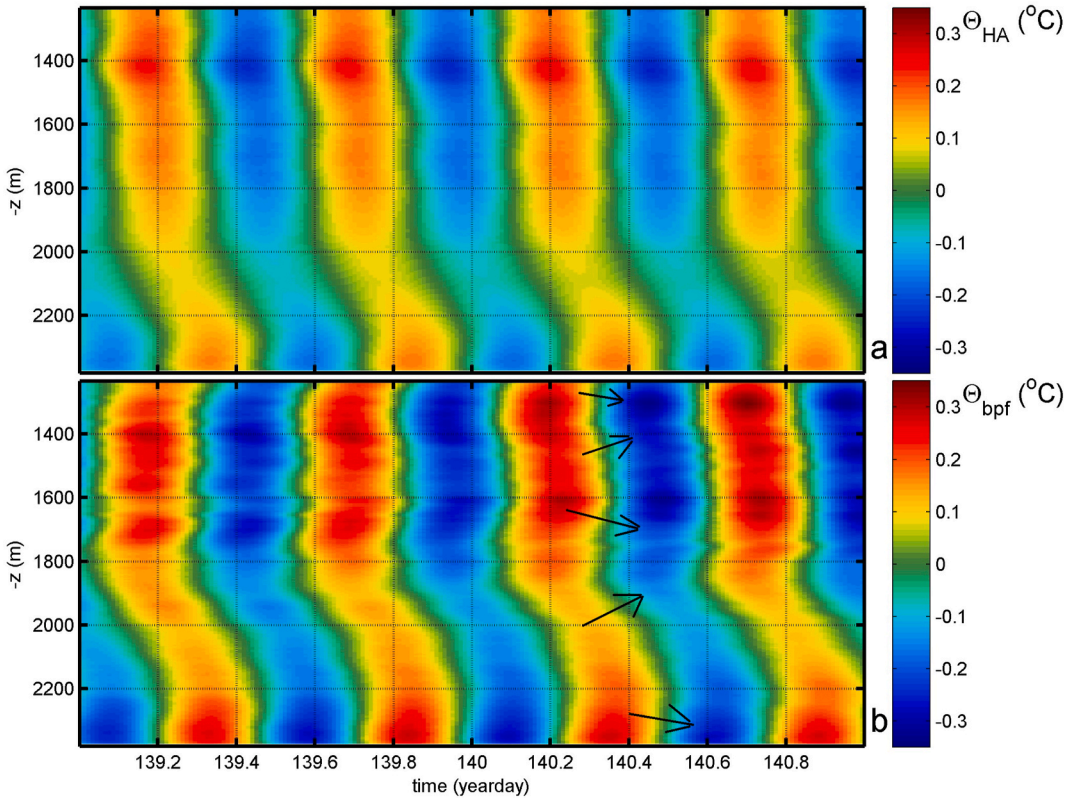

Fig. 6. Two days detail of SD-data from KmT-sensor data around spring tide, the same period as Fig. 2. (a) Harmonic data. (b) Bpf data.

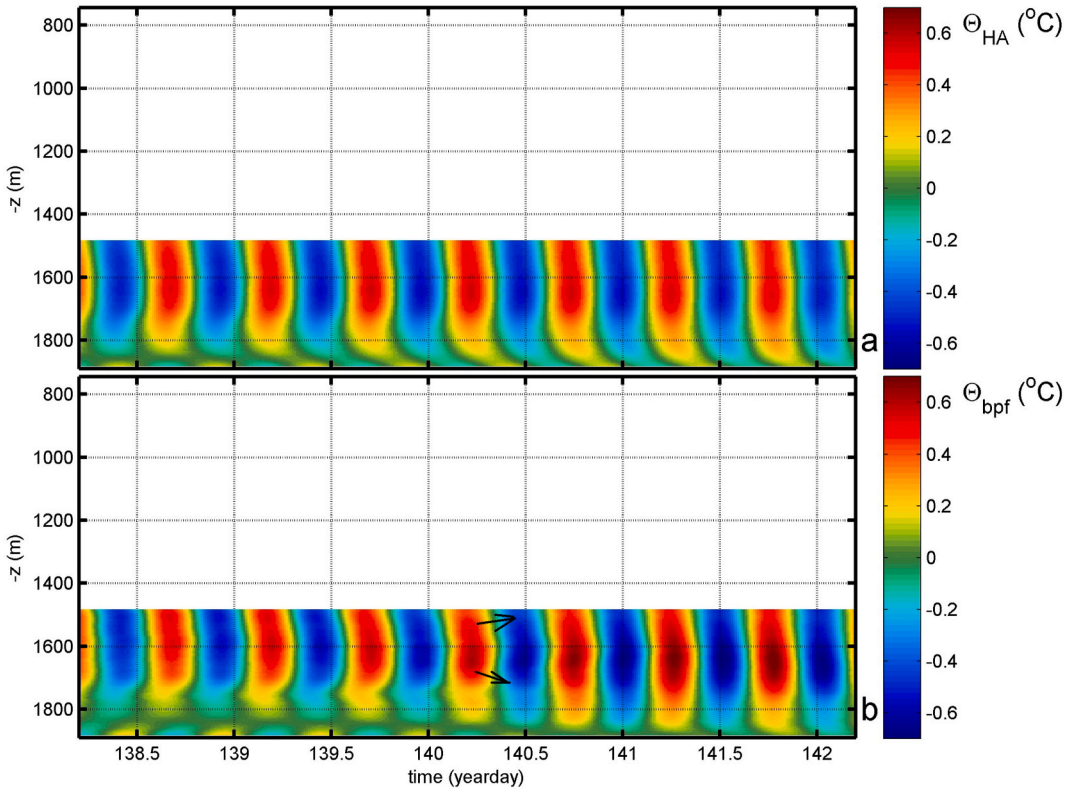

Fig. 7. Similar to Fig. 6, but for four days of data around spring-tide from a 400-m T-sensor array at z = −1890 m in 2015. Note the different colour scale compared with Fig. 6. The y-axis range is not reduced, for better comparison.

4. Discussion and conclusions

4.1. Vertical amplitude and phase variations of baroclinic tides

The KmT-observations show a dominant large, about 300-m scale baroclinic character of semidiurnal tidal motions, with noticeable small, 10-50-m scale baroclinic motions and negligible barotropic motions. These scales of motions are also observed in currents, which thus provide rather patchy time-vertical images. Not only amplitudes vary, but also the phases. Vertical phase differences of some 100° over about 400 m also have been observed in M_2-currents in the Bay of Biscay previously (Pingree and New, 1991; van Aken et al., 2007).

4.2. A cartoon of baroclinic energy propagation near a seamount

The vertical phase-variations can be interpreted in terms of internal wave propagation through a sufficiently stratified deep ocean. As sketched in a cartoon (Fig. 8), energy often propagates towards the ocean-floor in the lower 50–200 m, depending on the amount of wave breaking which is fed by the sloshing of the large-scale internal tide. Above this intense breaking-wave turbulence zone, energy propagates upward away from the slope, as if being generated by the non-linear waves and their breaking. Internal tide breaking does not occur continuously, but in pulses that are ±5% (semidiurnal) periodic with the main driver (van Haren, 2006). The largest pulse associates with an upslope propagating highly non-linear bore, occurring at the turn of warming to cooling phase of the sloshing tide. Such bores are accompanied by short and intense pulses of large vertical velocities and irregular small-scale waves superimposed on an asymmetric tidal signal. Their non-linearity is further exemplified by variations in frontal arrival and steepness, height, form, and which is communicated to the non-linear generation of internal tides. This occurs consistently each semidiurnal period during most energetic spring-tide.

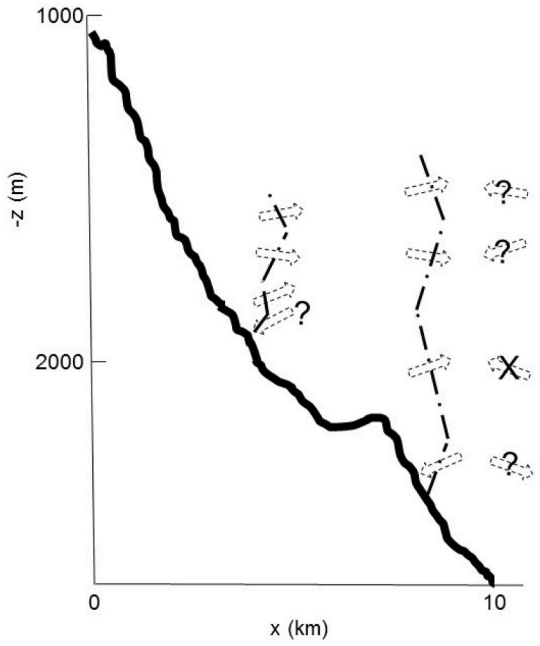

Fig. 8. Cartoon of internal wave propagation above a supercritical deep-sea slope during spring-tide. Dash-dot lines indicate vertical co-phase lines, inferred from Fig.. 6 and 7. The dashed arrows represent the direction of internal wave energy propagation inferred from the vertical phase variation. Upward energy propagation away from the slope seems to start at the top of large turbulence areas. Only vertical directions are determined, not the ambiguous horizontal as indicated by '?'. An 'X' implies unlikely horizontal direction after comparison with the other mooring results.

Such internal-wave generation by non-linear waves sloshing up- and down a slope has some resemblance with convective plumes impinging on the bottom of the near-surface mixing layer at the end of every night (Gregg et al., 1985; Moum et al., 1989). That convection-turbulence generates internal waves that propagate downwards into the interior. Here, the tidally periodic bursts of vertical motions associated with internal tide breaking (and non-linear bore formation) have much larger amplitudes than barotropic linear wave vertical tidal motions, which are normally considered to generate internal tides following flow-interaction with topography.

Higher up internal wave energy propagation alternates, across thinner layers when stratification increases. This leads to local divergence of energy, when a layer with upward propagation is above a layer with downward propagation. Local convergence of internal tide energy is expected when a layer with downward propagation is above one with upward propagation, such as around $z = -1800$ m. In the range $-1850 < z < -1600$ m, internal hydraulic jumps are observed, which are not related to flow over a sill but likely result from internal tide interaction.

It is noted that, unfortunately, horizontal propagation directions cannot be unambiguously established from the present 1D mooring data. The ADCP's u and v give particle velocities, not phase velocity (of wave propagation). In theory phase velocity can be obtained by investigating differences in the acoustic echo intensity in the different beams, but this provides only good results for an instrument fixed in space (instead of rotating in a mooring line), higher-resolution (instead of the coarse sampling in a 75 kHz LongRanger instrument), fast sampling (1 instead of 900 s per sample) and for small-scale well-defined features such as turbulent bores (but not internal tides) (van Haren, 2007). The ADCP's poor resolution in time and space, including its bad data in the lower 45 m above the seafloor, prevent quantitative comparison of energy-conversion rates via baroclinic and barotropic internal tide generation.

4.3. Qualitative effects of non-linear internal tide generation

The suggested non-linear internal tide source at the top of the breaker zone some distance above the ocean-floor disconnects internal wave generation from the precise topographic slope angle. This may explain previous ocean observations that internal tides are not necessarily generated over critical slopes where the topography slope matches that of the internal tide. Rather, steep supercritical slopes demonstrate stronger wave breaking and thus (part of) internal tide generation some distance above it. Such internal tide generation is then governed by stratification in the interior instead of that close to the ocean-floor. Once generated, internal wave propagation is not smooth as much as stratification is not constant but varying over thinner and thicker layers in space and time.

The non-linear source may be one explanation for the difficulty of observing internal wave beams in the ocean. First, internal tidal waves are not monochromatic, but generated over a finite bandwidth. Even if they were generated at only two frequencies, e.g. M_2 and S_2, their energy would spread through the ocean with separable characteristics as their slope-angles are different. Second, interactions of internal tides with stratification via local interior shear, reflection, breaking and isotherm straining (Alford and Pinkel, 2000) may generate interfacial waves, but certainly will attribute to intermittency via smearing over smaller scales.

As a result, even in the vicinity of large ocean-topography internal tide beams of characteristics have a patchy character as observed (van Haren et al., 2010). Likewise, interactions between internal tide beams and topography or thin-layer stratification unlikely yield freely propagating higher tidal harmonics, as modelled (e.g., Peacock and Tabaei, 2005; Diamessis et al., 2014). Such models do find (first) higher harmonics in their proper beams or near their source, but not throughout the deep ocean. This contrasts with common ocean observations of higher harmonics sequences at different fixed-point sites in a basin (e.g., van Haren et al., 2002; van Aken et al., 2007). Such observations likely

reflect forced non-resonant non-linear motions that are bound to the main, semidiurnal wave.

Declaration of competing interest

The authors declare that they have no known competing financial interests or personal relationships that could have appeared to influence the work reported in this paper.

Data availability

Data will be made available on request.

Acknowledgements

I thank the captain and crew of the R/V Pelagia and NIOZ-NMF for their very helpful assistance during deployment and recovery.

References

Alford, M.H., Pinkel, R., 2000. Overturning in the thermocline: the context of ocean mixing. J. Phys. Oceanogr. 30, 805–832.
Baines, P.G., 1982. On internal tide generation models. Deep-Sea Res. 29, 307–388.
Balmforth, N.J., Peacock, T., 2009. Tidal conversion by supercritical topography. J. Phys. Oceanogr. 39, 1965–1974.
Bell, T.H., 1975. Lee waves in stratified flows with simple harmonic time dependence. J. Fluid Mech. 67, 705–722.
Dale, A.C., Levine, M.D., Barth, J.A., Austin, J.A., 2006. A dye tracer reveals cross-shelf dispersion and interleaving on the Oregon shelf. Geophys. Res. Lett. 33, L03604 https://doi.org/10.1029/2005GL024959.
Dauxois, T., Joubaud, S., Odier, P., Venaille, A., 2017. Instabilities of internal gravity wave beams. Annu. Rev. Fluid Mech. 50, 131–156.
Diamessis, P.J., Wunsch, S., Delwiche, I., Richter, M.P., 2014. Nonlinear generation of harmonics through the interaction of an internal wave beam with a model oceanic pycnocline. Dynam. Atmos. Oceans 66, 110–137.
Dronkers, J.J., 1964. Tidal Computations in Rivers and Coastal Waters. North Holland Publishing Company, Amsterdam, the Netherlands.
Garrett, C., Kunze, E., 2007. Internal tide generation in deep ocean. Annu. Rev. Fluid Mech. 39, 57–87.
Gerkema, T., 2002. Application of an internal tide generation model to baroclinic spring-neap cycles. J. Geophys. Res. 107, 3124. https://doi.org/10.1029/2001JC001177.
Gerkema, T., Lam, F.P.A., Maas, L.R.M., 2004. Internal tides in the Bay of Biscay: conversion rates and seasonal effects. Deep Sea Res. II 51, 2995–3008.
Gregg, M.C., Peters, H., Wesson, J.C., Oakey, N.S., Shay, T.J., 1985. Intensive measurements of turbulence and shear in the equatorial undercurrent. Nature 318, 140–144.
Grue, J., Jensen, A., Rusas, P.O., Sveen, K.J., 2000. Breaking and broadening of internal solitary waves. J. Fluid Mech. 413, 181–217.
Hebert, D., Oakey, N., Ruddick, B., 1990. Evolution of a Mediterranean salt lens: scalar properties. J. Phys. Oceanogr. 20, 1468–1483.
Hosegood, P., Bonnin, J., van Haren, H., 2004. Solibore-induced sediment resuspension in the faeroe-shetland channel. Geophys. Res. Lett. 31, L09301 https://doi.org/10.1029/2004GL019544.
IOC, SCOR, IAPSO, 2010. The International Thermodynamic Equation of Seawater – 2010: Calculation and Use of Thermodynamic Properties, Intergovernmental Oceanographic Commission, Manuals and Guides No. 56. UNESCO, Paris, France.
Johnston, T.M.S., Rudnick, D.L., Carter, G.S., Todd, R.E., Cole, S.T., 2011. Internal tidal beams and mixing near Monterey Bay. J. Geophys. Res. 116, C03017 https://doi.org/10.1029/2010JC006592.
Klymak, J.M., Moum, J.N., 2003. Internal solitary waves of elevation advancing on a shoaling shelf. Geophys. Res. Lett. 30, 2045. https://doi.org/10.1029/2003GL017706.
Lamb, K.G., 2004. Nonlinear interaction among internal wave beams generated by tidal flow over supercritical topography. Geophys. Res. Lett. 31, L09313 https://doi.org/10.1029/2003GL019393.
LeBlond, P.H., Mysak, L.A., 1978. Waves in the Ocean. Elsevier, New York, USA.
Legg, S., Klymak, J., 2008. Internal hydraulic jumps and overturning generated by tidal flow over a tall steep ridge. J. Phys. Oceanogr. 38, 1949–1964.
Lien, R.-C., Gregg, M.C., 2001. Observations of turbulence in a tidal beam and across a coastal ridge. J. Geophys. Res. 106, 4575–4591.
Moum, J.N., Caldwell, D.R., Paulson, C.A., 1989. Mixing in the equatorial surface layer and thermocline. J. Geophys. Res. 94, 2005–2021.
Mowbray, D.E., Rarity, B.S.H., 1967. A theoretical and experimental investigation of the phase configuration of internal waves of small amplitude in a density stratified liquid. J. Fluid Mech. 28, 1–16.
Pawlowicz, R., Beardsley, B., Lentz, S., 2002. Classical tidal harmonic analysis including error estimates in MATLAB using T_TIDE. Comput. Geosci. 28, 929–937.
Peacock, T., Tabaei, A., 2005. Visualization of nonlinear effects in reflecting internal wave beams. Phys. Fluids 17, 061702.
Pingree, R.D., New, A.L., 1991. Abyssal penetration and bottom reflection of internal tide energy in the Bay of Biscay. J. Phys. Oceanogr. 21, 28–39.
Sarkar, S., Scotti, A., 2017. From topographic internal gravity waves to turbulence. Annu. Rev. Fluid Mech. 49, 195–220.
Slinn, D.N., Riley, J.J., 1996. Turbulent mixing in the oceanic boundary layer caused by internal wave reflection from sloping terrain. Dynam. Atmos. Oceans 24, 51–62.
Smith, W.H.F., Sandwell, D.T., 1997. Global ocean-floor topography from satellite altimetry and ship depth soundings. Science 277, 1957–1962.
Sutherland, B.R., 2013. The wave instability pathway to turbulence. J. Fluid Mech. 724, 1–4.
Thorpe, S.A., 1977. Turbulence and mixing in a Scottish loch. Phil. Trans. Roy. Soc. Lond. 286, 125–181.
van Aken, H.M., van Haren, H., Maas, L.R.M., 2007. The high-resolution vertical structure of internal tides and near-inertial waves, measured with an ADCP over the continental slope in the Bay of Biscay. Deep-Sea Res. I 54, 533–556.
van Haren, H., 2006. Nonlinear motions at the internal tide source. Geophys. Res. Lett. 33, L11605 https://doi.org/10.1029/2006GL025851.
van Haren, H., 2007. Echo intensity data as a directional antenna for observing processes above sloping ocean bottoms. Ocean Dynam. 57, 135–149.
van Haren, H., 2017. Exploring the vertical extent of breaking internal wave turbulence above deep-sea topography. Dynam. Atmos. Oceans 77, 89–99.
van Haren, H., 2018. Philosophy and application of high-resolution temperature sensors for stratified waters. Sensors 18, 3184. https://doi.org/10.3390/s18103184.
van Haren, H., 2022. KmT, kilometer-long mooring of high-resolution temperature measurements results overview. Dynam. Atmos. Oceans 100, 101336.
van Haren, H., Maas, L., 2022. A simple model for an internal wave spectrum dominated by non-linear interactions. Tellus 74, 382–390.
van Haren, H., Maas, L., van Aken, H., 2002. On the nature of internal wave spectra near a continental slope. Geophys. Res. Lett. 29 (12) https://doi.org/10.1029/2001GL014341.
van Haren, H., Maas, L.R.M., Gerkema, T., 2010. Patchiness in internal tidal beams. J. Mar. Res. 68, 237–257.
van Haren, H., Cimatoribus, A., Gostiaux, L., 2015. Where large deep-ocean waves break. Geophys. Res. Lett. 42, 2351–2357. https://doi.org/10.1002/2015GL063329.
Winters, K.B., 2015. Tidally driven mixing and dissipation in the boundary layer above steep submarine topography. Geophys. Res. Lett. 42, 7123–7130. https://doi.org/10.1002/2015GL064676.
Wunsch, C., 1975. Internal tides in the ocean. Rev. Geophys. 13, 167–182.